Received: 4 December 2023 | Revised: 1 July 2024 | Accepted: 3 July 2024

IET Microwaves, Antennas & Propagation

DOI: 10.1049/mia2.12494

ORIGINAL RESEARCH

# Multi-band millimetre wave indoor directional channel measurements and analysis for future wireless communication systems

**Amar Al-Jzari** | **Sana Salous**

Engineering Department, University of Durham, Durham, UK

**Correspondence**

Sana Salous.
Email: sana.salous@durham.ac.uk

**Funding information**

H2020 Marie Sklodowska-Curie Actions, Grant/Award Number: 766231; Engineering and Physical Sciences Research Council, Grant/Award Numbers: mmWaveTRACCS, EP/W027151/1, PATRICIAN, EP/I00923X/1

**Abstract**

Single-input single-output (SISO) three-dimensional (3D) wideband indoor directional measurements collected in a factory environment and an office environment at 38 and 70 GHz are presented. 3D single-input multiple-output (SIMO) dual polarised measurements with 1 × 2 antenna configurations were also carried out in a meeting room, a conference room, and an office room at the 60 GHz band. The measurements cover both azimuth and elevation by rotating the directional antenna (RDA) at the receiver side. Different statistical channel parameters such as power delay profile, power angle profile, root-mean-square delay spread, angular spread, and path loss were estimated for different possible antenna orientations between the transmitter and the receiver, which include line-of-sight, obstructed line-of-sight, and non-line-of-sight. The polarisation effects on path loss models and the delay and angular spread models based on the surface area of the environment are studied. The results will be valuable for the design of indoor millimetre wave cellular networks.

**KEYWORDS**

millimetre wave communication, millimetre wave propagation

## 1 | INTRODUCTION

The increasing demand for high data rate transmission has prompted the wireless industry, academics, and regulators to consider scaling up to the millimetre wave (mmWave) spectrum. The mmWave band with a large transmission bandwidth (BW) is viewed as a key technology for fifth generation (5G) wireless systems, which considerably extend the channel capacity of indoor wireless networks [1, 2]. Whilst mmWave communication offers high data rates, due to its small wavelengths, it will have widely different propagation channel characteristics compared with the sub-6 GHz frequency bands, such as high propagation loss, the weakest reliable diffraction mechanism, and susceptibility to shadowing (e.g. blockage by humans or obstacles). Instead of using omni-directional antennas, highly directional antennas will be employed to compensate for the high PL. MmWave can only be used over a very short distance as a result of its high penetration loss. Accordingly, adaptive beamforming is a promising technology that can be used to overcome the high loss due to its high directivity [3]. Therefore, directional channel measurements in various indoor environments at these frequency bands are essential for a good understanding of the propagation characteristics and providing reliable channel models for the robust design of radio networks.

Several channel measurements have been reported at mmWave bands in different environments following the world radio communications conference in 2015 (WRC15) which identified several mmWave bands for 5G networks. In refs. [4, 5], channel measurements were conducted at 15, 28, 60, and 70 GHz bands in several environments, such as offices, station, shopping mall, and airport. Both line-of-sight (LoS) and non-line-of-sight (NLoS) scenarios were considered and different relevant channel parameters were estimated, such as power delay profile (PDP), power angle profile (PAP), azimuth and elevation angular spread (AS), root-mean-square delay spread

(RMS DS), path loss (PL), and cross-polarisation ratio (XPR). In refs. [6, 7], directional channel measurements within a typical indoor office environment were conducted at 28 and 73 GHz using a sliding correlator channel sounder. Large-scale propagation PL models and the RMS DS statistics were obtained. In refs. [8, 9], wideband directional channel measurements were conducted at 62 and 83 GHz in office room and conference room environments using a vector network analyser (VNA) and two horn antennas. Different multipath component parameters (MPCs), including PDP, PAP, RMS DS, and PL models, angle of arrival (AoA), and angle of departure (AoD) spreads were investigated. In refs. [10, 11], V-band directional dual polarised measurements were conducted in indoor and outdoor environments using a multi-band chirp-based channel sounder. The impact of polarisation on several channel parameters were investigated. In refs. [12, 13], directional channel measurements were conducted in various outdoor environments using a chirp-based channel sounder with horn antennas at the transmitter (Tx) and receiver (Rx). The investigated channel statistical properties include PDP, RMS DS, and PL. In ref. [14], 60 GHz indoor channel measurements were performed using a VNA with an omni-directional antenna or a horn antenna at the Tx and a horn antenna at the Rx. The MPCs parameters, including PDP, PAP, RMS DS, and AS, were obtained. In ref. [15], indoor office channel measurements were conducted at 11, 16, 28, and 38 GHz using a VNA. The channel statistical properties, including PDP, PAP, RMS DS, azimuth AS, elevation AS, channel capacity, and correlation properties were estimated. In ref. [16], three types of office room environments were measured at 45 GHz using a VNA and signal generator. Channel characteristics such as PL, path loss exponent (PLE), shadow fading (SF) deviation, and cross-polarisation discrimination ratio were thoroughly analysed. In ref. [17], a VNA with an omni-directional biconical antenna at the Tx and a horn antenna at the Rx were used to measure 26 and 38 GHz in a corridor and a stairwell. The RMS DS statistics, SF, and PL models were obtained for both LoS and NLoS scenarios. In refs. [18, 19], several types of indoor environments were measured at 26 and 28 GHz to estimate the channel parameters of the MPCs. In ref. [20], SISO and MIMO channel measurements were conducted in indoor office environment at different frequency bands using a Keysight time domain channel sounder to investigate the large-scale fading and small-scale fading of wireless channels. Multi-frequency wireless channel characteristics were obtained. In ref. [21], various indoor environments were measured at the Ka-band of the mmWave spectrum using a chirp channel sounder. The large-scale fading, RMS DS, and verification of indoor channel simulations based on ray tracing at this band were presented and analysed. In ref. [22], multi-frequency multi-scenario mmWave channel measurements were conducted at 28, 32, and 39 GHz using a time domain channel sounder. The channel statistical properties, including PDP, PL, PLE, RMS DS, and blockage effects, were thoroughly studied. In refs. [23, 24], multi-frequency mmWave and sub-Terahertz propagation analysis in large office and corridor environments were conducted at 28, 38, 71, 82, and 159 GHz based on real-time omni-directional channel measurements. Multi-band propagation characteristics, including PL models, SF distribution, and RMS DS, were obtained. In refs. [25, 26], mmWave and sub-Terahertz channel measurements were conducted in indoor office building environment at 28, 73, and 140 GHz using a sliding correlator channel sounder. The large-scale fading and the multipath time dispersion parameters were obtained and compared.

Despite these numerous studies, three-dimensional (3D) directional multi-band measurements at 39 and 70 GHz are limited and seldom reported in environments such as a factory or industrial scenario as well as office scenario. There is a great deal of interest in the propagation effects in industrial environments as they present several reflective surfaces, which can lead to considerable reflections compared with conventional environments. Therefore, measurements are needed, as the majority of earlier research used ray tracing simulation tools as to perform theoretical analysis of this type of environment. In addition, to the best of our knowledge, a model for predicating the delay and angular spread values as a function of the room size at V-band was generated for the first time based on ITU-R P.1238 for different antenna alignments and different polarisation links.

In this work, single-input single-output (SISO) 3D wideband channel measurements are carried out in factory and office environments at 39 and 70 GHz by rotating a directional antenna (RDA). Wideband channel parameters such as RMS DS, average PDPs, PAP, AS, and PL models are estimated for different angular directions between the Tx and the Rx antennas. Moreover, single-input multiple-output (SIMO) 3D dual polarised measurements are conducted in the 60 GHz band in a meeting room, a conference room, and an office room. The propagation channel characteristics are estimated for different angular orientations and different polarisation links.

The rest of the paper is organised as follows. Section 2 describes the measurement environment and the measurements procedures. Section 3 describes the statistical channel characteristics. Measurements and modelling results and analysis are provided in Section 4. Finally, conclusions are drawn in Section 5.

## 2 | MEASUREMENT METHODOLOGY

This section introduces the directional wideband channel measurement, including the specification of the channel sounding equipment, measurement environment, and measurement deployment.

### 2.1 | SISO directional measurements

A custom-designed Durham University's channel sounder [27, 28] was used to conduct SISO 3D indoor directional channel measurements in factory and office environments shown in Figure 1a, with the corresponding Tx and Rx locations in Figure 1b. At a repetition frequency of 1.22 kHz, the

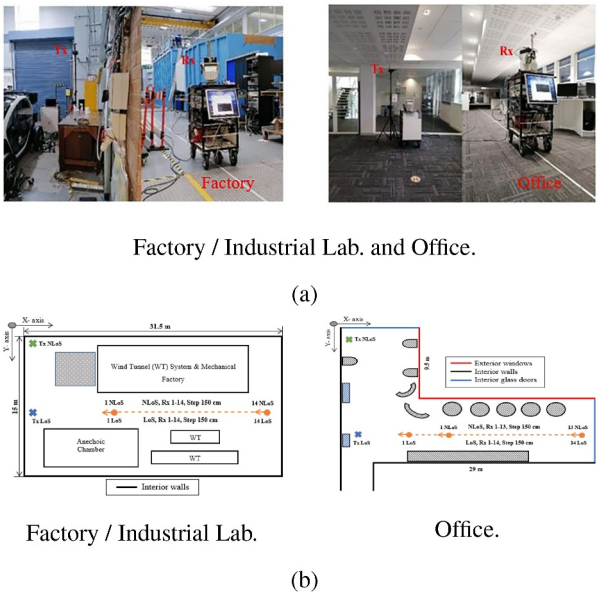


**FIGURE 1** SISO measurement environments. (a) Photos of the factory and office scenarios. (b) Layouts of the factory and office scenarios.

measurements were carried out with 4.5 and 6 GHz bandwidths centred at 38.31 and 70.28 GHz, respectively. An omni-directional antenna is used at the Tx, while a horn antenna with a typical gain of 20 dBi (~18° HPBW) was employed at the Rx. For both LoS and NLoS scenarios, the Tx antenna was fixed and placed at one end of the measured environment, while the Rx antenna was moved to specified locations within the scenario, as shown in Figure 1b. The Tx antenna was supported by a tripod at a height of 2.4–3 m above the ground level, while the Rx antenna was set up at 1.6–1.7 m to emulate a typical WLAN network environment. To investigate the directional channel parameters in the angular domain, a positioner rotates the horn antenna at the receiver from 0° to 360° with a step of 10° in the azimuth plane and from −15° to 15° with a step of 15° in the elevation plane to estimate the angle of arrival (AoA). Therefore, 108 data files were recorded at each location, corresponding to the different Rx antenna pointing angles in azimuth and elevation. At each angular rotation, the data were recorded for one second duration. Table 1 provides a summary of the channel sounder set-up parameters for the SISO directional measurements.

## 2.2 | SIMO directional measurements

SIMO dual polarised channel measurements with 1 × 2 antenna configurations were conducted in a meeting room, a conference room, and an office room environments, as shown in Figure 2a. The measured environments are furnished with many chairs, desks, tables, and computers. An omni-directional antenna was used at the Tx, while at the Rx, two horn antennas with different polarisations (vertical—horizontal (V—H)) were used to investigate the impact of polarisation on the propagation channel characteristics. The measurements were conducted in a LoS scenario with the Tx location fixed at one end of the room while the Rx was relocated onto predefined

**TABLE 1** SISO Channel measurements set-up parameters.

| RF centre freq. | 38.31 GHz | 62.6 GHz | 70.28 GHz |
|---|---|---|---|
| RF bandwidth | 4.5 GHz | 6 GHz | |
| Analysis bandwidth | 1.5 GHz | 2 GHz | |
| Sampling rate | 40 MHz | | |
| Sweep rate | 1.22 kHz | | |
| Record duration | 1 s | | |
| Antenna Configuration | 1 × 1 (SISO) | | |
| Tx antenna type | Omni-directional antenna | | |
| Rx antenna type | Standard horn antenna (20 dBi gain and 18° HPBW) | | |
| Tx/Rx polarisation | Vertical-vertical (V—V) | | |
| Tx antenna height | 2.4–3 m | | |
| Rx antenna height | 1.6–1.7 m | | |

locations within the scenario, as shown in Figure 2b. The arrow at the Rx position represents the main beam's direction at a rotation angle of 0°. The Tx antenna height was set close to the typical height of an access point, while the Rx antenna height was set to the typical average height of a user. A rotator is used at the receiver to steer the directional antennas from 0° to 360° with a step of 10° in azimuth and from −15° to 15° with a step of 15° in elevation. Table 2 gives a summary of the SIMO channel measurement set-up parameters.

# 3 | CHANNEL STATISTICAL CHARACTERISTICS AND MODELLING

This section describes various wideband channel parameters. Additionally, path loss models and the delay and angular spread models are presented.

## 3.1 | Channel parameters

The measured PDP is expressed as follows:

$$\mathrm{PDP} = P(\tau) = \frac{1}{M}\sum_{m=1}^{M} |h_m(t_m, \tau)|^2 \quad (1)$$

where $M$ is the total number of channel impulse response (CIR) snapshots captured in each measured position within the acquisition period and $\tau$ is the time delay. The measured PDP was then used to estimate different relative channel parameters.

The RMS DS is the square root of the second central moment of the PDP and can be calculated as follows:

$$\tau_{rms} = \sqrt{\frac{\sum_{n=1}^{N} P_n \tau_n^2}{\sum_{n=1}^{N} P_n} - \left(\frac{\sum_{n=1}^{N} P_n \tau_n}{\sum_{n=1}^{N} P_n}\right)^2} \quad (2)$$

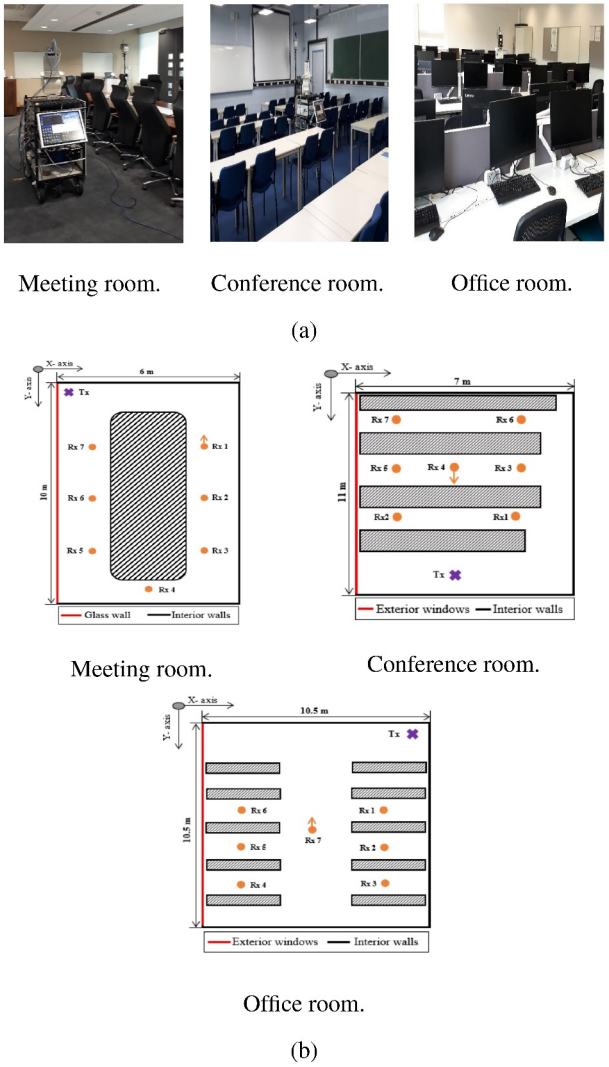


**FIGURE 2** SIMO measurement environments. (a) Photos of the meeting room, conference room, and office room scenarios. (b) Layouts of the meeting room, conference room and office room scenarios.

**TABLE 2** SIMO Channel measurements set-up parameters.

| **RF centre freq.** | **62.6 GHz** |
|---|---|
| RF bandwidth | 6 GHz |
| Analysis bandwidth | 2 GHz |
| Sampling rate | 40 MHz |
| Sweep rate | 1.22 kHz |
| Record duration | 1 s |
| Antenna Configuration | 1 × 2 (SIMO) |
| Tx antenna type | Omni-directional antenna |
| Rx antenna type | Standard horn antenna (20 dBi gain and 18° HPBW) |
| Tx/Rx polarisation | (V—V) and (V—H) |
| Tx antenna height | 2.4–2.6 m |
| Rx antenna height | 1.6 m |

where $N$ is the number of MPCs, $\tau_n$ and $P_n$ are the delay and the power of the $n$th path, respectively.

The AS is used to characterise the dispersion properties of the PAP and can be calculated as follows:

$$\mathrm{PAP} = P_R(\theta_K) = \sum_{n=1}^{N} P(\tau_n, \theta_K) \tag{3}$$

$$\theta_m = \arg\left(\frac{\sum_{k=1}^{K} P_R(\theta_K)\exp^{j\theta_K}}{\sum_{k=1}^{K} P_R(\theta_K)}\right) \tag{4}$$

$$\mathrm{AS} = \theta_{AS} = \sqrt{\frac{\sum_{k=1}^{K} P_R(\theta_K)\left((\theta_K - \theta_m)^2\right)}{\sum_{k=1}^{K} P_R(\theta_K)}} \tag{5}$$

where $\theta_m$ is the mean azimuthal angle of arrival or departure, $K$ is the total number of angles per location, and $P_R(\theta_K)$ is the PAP (represents the received power at each azimuth angle $\theta_K$, given in Equation (3) as the sum of the corresponding noise free PDP). $\theta_K$ is restricted to the range of $+/-\ \pi$.

The PL represents the ratio between the transmitted power ($P_{Tx}$) and the received power ($P_{Rx}$) without the overall system gain and antenna gains. The PL can be defined as follows:

$$\mathrm{PL[dB]} = P_{Tx} + G_{Rx} + G_{Tx} - P_{Rx} - L_{Sy} \tag{6}$$

$$P_{Rx} = \sum_{n=1}^{N} P_n \tag{7}$$

where $L_{Sy}$ is the overall system loss in dB. $G_{Tx}$ and $G_{Rx}$ are the Tx and the Rx antenna gains, respectively.

## 3.2 | PL models

Two single-frequency PL models: the close-in (CI) model and the log-distance (Floating-intercept (FI)) model, have been commonly used to provide the best fit for the measured data. The CI model expressed in Equation (8) represents the simplest model since the PL dependence on the distance is described by a single dimensionless PL coefficient ($\alpha$) and a fixed offset. The FI model given in Equation (9) estimates two parameters including the PL intercept coefficient ($\beta$) in dB and the dimensionless PL coefficient ($\alpha$).

$$\mathrm{PL}_{CI}(d)[\mathrm{dB}] = 20\log_{10}(f_\circ) - 27.5 + 10\alpha\log_{10}(d) + X_\sigma^{CI} \tag{8}$$

$$\mathrm{PL}_{FI}(d)[\mathrm{dB}] = \beta + 10\alpha\log_{10}(d) + X_\sigma^{FI} \tag{9}$$

where $f_\circ$ is the operating frequency in MHz, $d$ is the three-dimensional (3D) distance in metre (m) between the Tx and

the Rx antennas, and $X_{\sigma}^{CI}$ and $X_{\sigma}^{FI}$ are Gaussian distributions with zero mean and variance equal to the standard deviation $\sigma$(dB).

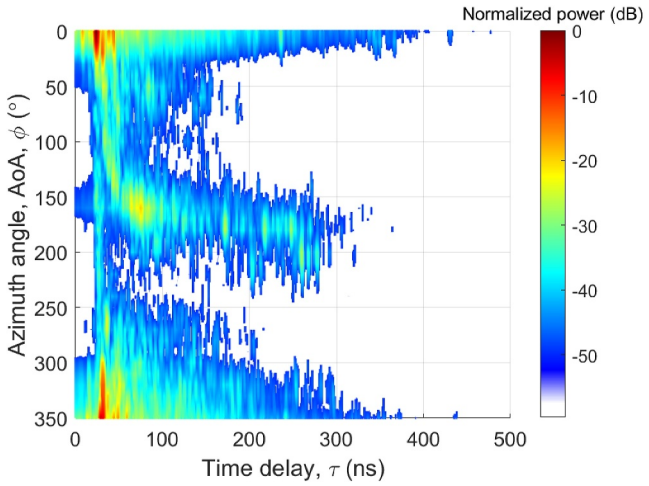


**FIGURE 3** Relative PDP versus Rx rotation angle for LoS scenario at a 15-degree elevation angle at 38 GHz.

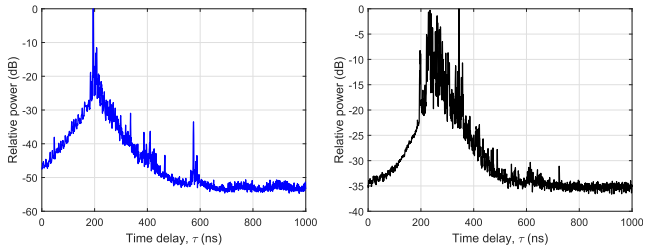


(a) LoS angle (b) OLoS angle.

**FIGURE 4** PDPs at different azimuth angles for LoS scenario at a 15-degree elevation angle at 38 GHz.

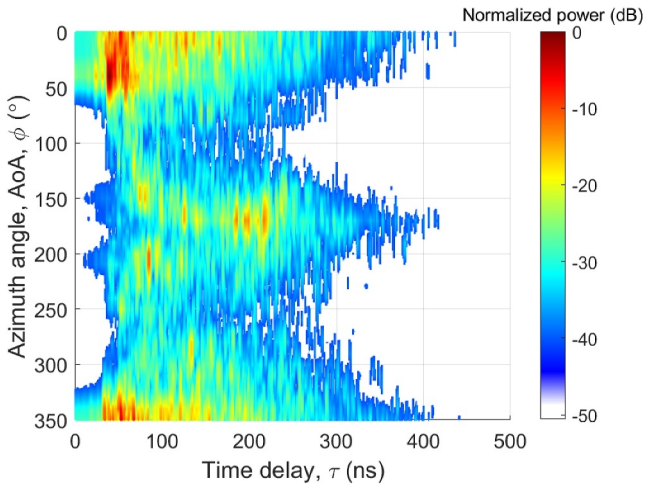


**FIGURE 5** Relative PDP versus Rx rotation angle for NLoS scenario at a 15-degree elevation angle at 38 GHz.

## 3.3 | Delay and angular spread models

The RMS DS and AS are predicted based on the surface area of the measured environment. A model for the delay spread and the angular spread values as a function of the room size are given in Equations (10) and (11), which are based on the ITU delay spread model described in ref. [29].

$$10\log_{10}(\mathrm{DS}) = \alpha\log_{10}(\mathrm{F}_s) + \beta \tag{10}$$

$$10\log_{10}(\mathrm{AS}) = \alpha\log_{10}(\mathrm{F}_s) + \beta \tag{11}$$

where $\mathrm{F}_s$ is the area of the floor space in $\mathrm{m}^2$, $\alpha$ and $\beta$ are the model coefficients, DS is the RMS delay spread in ns, and AS is the angular spread in degrees.

# 4 | RESULTS AND ANALYSIS

This section discusses the results and analysis of the mmWave directional channel measuremens conducted in the indoor environments.

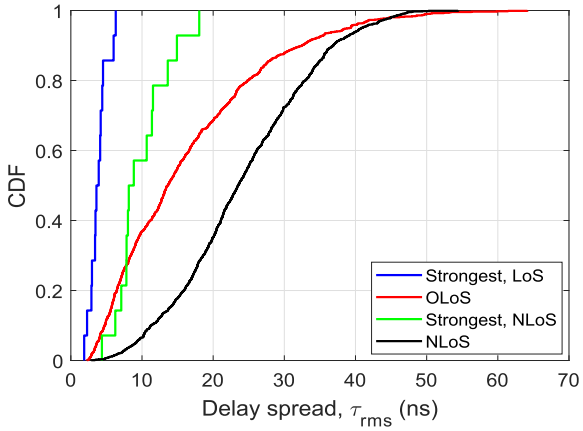


(a) 38.31 GHz.

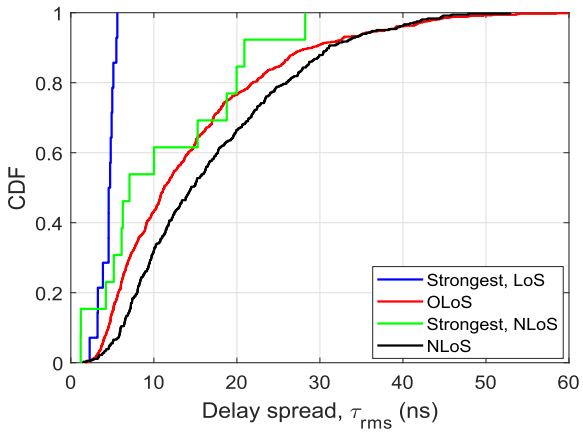


(b) 70.28 GHz.

**FIGURE 6** CDF of RMS DS for the factory environment.

## 4.1 | SISO directional channel measurements and modelling results

### 4.1.1 | Directional PDP

Figure 3 presents an example of the normalised PDP at 38 GHz for a LoS location in the factory environment as a function of the Rx azimuth angle. The colourmap minimum was adjusted to 10 dB above the noise level. The figure shows that the strong LoS component is received in the boresight (BS) angles at around 0° and 350° within 25 ns when the Rx antenna was oriented towards the Tx antenna. Another peak appears at around 180° between 250 and 400 ns, which corresponds to reflections from a concrete wall at the end of the measured environment. According to the Rx deployment in Figure 1b, multipath reflections can be seen between 0° and 150° caused by reflections from the wind tunnel (WT) to the right of the Rx and between 250° and 350° caused by reflections from the anechoic chamber to the left of the Rx. These reflected components appeared when the Rx antenna was pointed away from the Tx antenna. The large number of reflections emphasises the reflecting nature of this environment, which is full of metallic surfaces as seen in Figure 1a. The impact of beam alignment can be further seen in Figure 4. This figure displays the PDP of the BS angle when the Tx and Rx antenna main beams are aligned as well as the PDP of the non-boresight (NBS) (obstructed LoS (OLoS)) angle when the main beams are not aligned.

Figure 5 presents an example of the normalised PDP at 38 GHz of one NLoS location versus the Rx azimuth rotation angle. More MPCs can be observed at various rotation angles within different time delays due to the larger number of reflections within the environment, leading to a large delay spread compared with the LoS location. Two strong signal components can be seen, one between 0° and ~50° and the other between ~320° and ~350°, which corresponds to the reflections from the WT and the anechoic chamber surfaces based on the Rx deployment in Figure 1b. Other multipath reflections with lower power levels can be detected between ~60° and ~310°, induced by the reflections within the scenario when the Rx antenna was oriented at different azimuth angles. In addition, Figures 4 and 5 illustrate the angular power spectrum between sources of the MPCs by mapping the power level to the Rx deployment in the environment, as previously mentioned.

### 4.1.2 | RMS DS

The RMS DS was estimated with a 20 dB threshold. Figure 6 displays the CDFs of the RMS DS for the industrial environment, where the estimated delay spread was classified as LoS when the Rx antenna was pointing towards the Tx antenna, OLoS when the Rx antenna was physically in the LoS of the Tx but the antenna beam was misaligned with the Tx antenna, and NLoS when the Rx and Tx antennas were obstructed, as shown in Figure 1b. This can be seen in both measured frequency bands, the increase in the RMS DS values of the OLoS and NLoS scenarios due to the misalignment of the antenna beams and the presence of the obstruction. The CDF of the RMS DS for the angles with the maximum received power was also provided for both LoS and NLoS cases. The results

**TABLE 3** RMS DS statistics in [ns] for the factory (office) environments.

| Freq. GHz | CDF of RMS DS | Measured scenario | | | |
|---|---|---|---|---|---|
| | | Strongest LoS | OLoS | Strongest NLoS | NLoS |
| 38.31 | 10% | 2.037 | 4.739 | 5.118 | 11.229 |
| | | (2.134) | (3.256) | (1.588) | (7.197) |
| | 50% | 3.597 | 13.561 | 8.144 | 23.495 |
| | | (3.154) | (8.202) | (4.258) | (15.124) |
| | 90% | 5.416 | 32.483 | 14.393 | 36.878 |
| | | (4.735) | (28.209) | (13.003) | (23.425) |
| | $\sigma_{rms}$ | 1.246 | 11.111 | 3.711 | 9.618 |
| | | (0.988) | (10.666) | (4.788) | (7.311) |
| 70.28 | 10% | 2.647 | 4.505 | 1.190 | 5.990 |
| | | (0.474) | (3.076) | (0.419) | (1.251) |
| | 50% | 4.557 | 11.244 | 6.661 | 14.490 |
| | | (4.071) | (9.568) | (7.316) | (10.339) |
| | 90% | 5.338 | 28.902 | 20.620 | 30.994 |
| | | (7.218) | (29.533) | (15.850) | (17.219) |
| | $\sigma_{rms}$ | 0.946 | 10.542 | 8.607 | 10.221 |
| | | (2.825) | (10.918) | (6.349) | (6.144) |

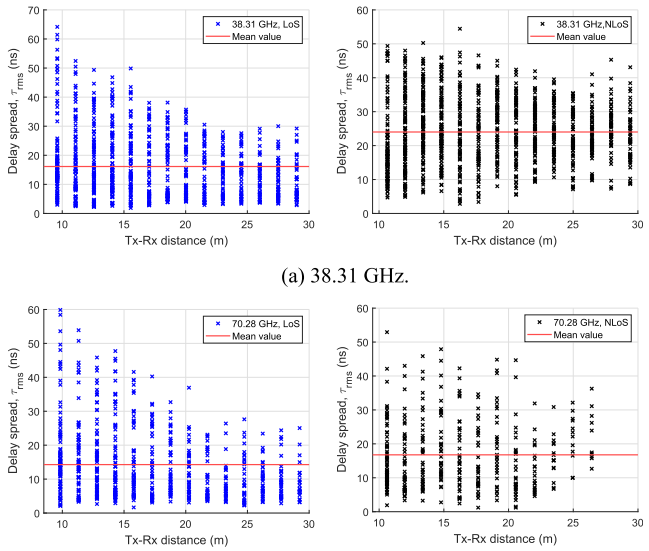


(a) 38.31 GHz.

(b) 70.28 GHz.

**FIGURE 7** RMS DS values versus Tx-Rx distance for the factory environment.

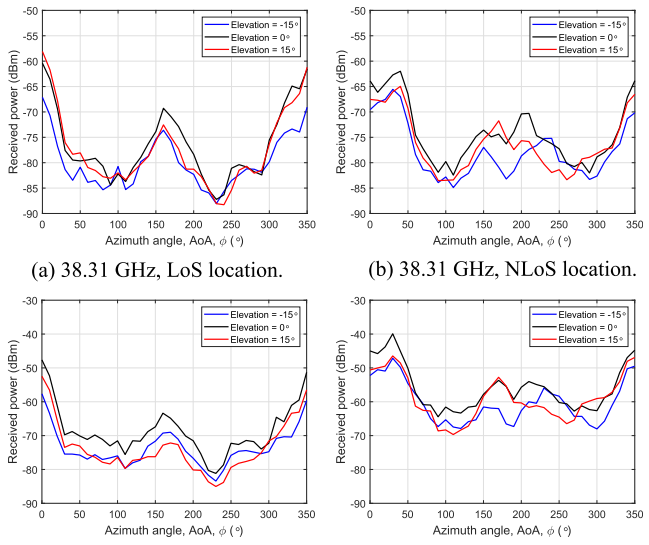


(a) 38.31 GHz, LoS location.

(b) 38.31 GHz, NLoS location.

(a) 70.28 GHz, LoS location.

(b) 70.28 GHz, NLoS location.

**FIGURE 8** Power angle profile for LoS and NLoS scenarios in the factory environment.

indicate that the strongest angle beams have substantially lower delay spread values compared with the arbitrary pointing angle beams, since the strongest received power angle may have the main LoS component as well as a very weak multipath component. These observations imply that using the beam steering approach will be beneficial to minimise delay spread. The 10%, 50%, and 90% CDF values of the RMS DS, as well as the corresponding standard deviation ($\sigma_{rms}$) for each scenario, are given in Table 3. This table indicates that the maximum difference varied in the range of 0.92–9 ns between

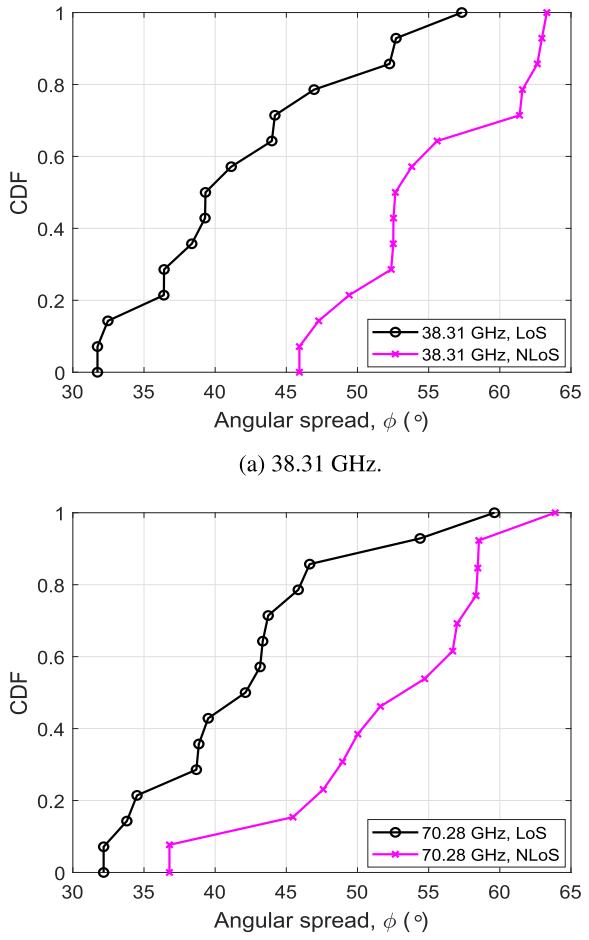


(a) 38.31 GHz.

(b) 70.28 GHz.

**FIGURE 9** CDF of AS for the factory environment.

the two bands for 50% and 90% of the CDF values across all the measured scenarios in both environments. The table also shows that the 70 GHz band has smaller delay spread values than the 38 GHz band, by comparing the 50% CDF values across the measured scenarios. Moreover, the ($\sigma_{rms}$) values across all the scenarios for both environments at both bands are less than 12 ns. Similar RMS DS statistics were reported at 70 GHz [4–11] and 38 GHz [16, 17].

Figure 7 displays the directional RMS DS versus the Tx-Rx separation distance at the industrial environment, for both LoS and NLoS scenarios at 38 and 70 GHz bands. The computed mean delay spread values for the industrial environment across all the distances in the LoS scenario are 16.14 and 14.28 ns for 38 and 70 GHz, respectively. The NLoS scenario exhibited higher mean delay spread values of 24.01 and 16.76 ns for 38 and 70 GHz, respectively. Furthermore, the mean delay spread values in the office environment over all distances in the LoS and NLoS situations varied in the range of 12–14 ns and 10–13 ns for 38 and 70 GHz, respectively. The results also showed that the estimated RMS DS values followed a decreasing trend when the separation distance increased.

**TABLE 4** AS statistics in [degrees] for the factory (office) environments.

| | | Measured scenario | |
|---|---|---|---|
| **Freq. GHz** | **CDF of AS** | **LoS** | **NLoS** |
| 38.31 | 10% | 32.025 | 46.461 |
| | | (31.194) | (41.793) |
| | 50% | 39.319 | 52.662 |
| | | (64.623) | (53.387) |
| | 90% | 52.526 | 62.829 |
| | | (102.854) | (75.763) |
| | $\sigma_{\theta_{AS}}$ | 7.717 | 6.035 |
| | | (26.521) | (11.837) |
| 70.28 | 10% | 32.816 | 39.391 |
| | | (27.063) | (33.348) |
| | 50% | 42.127 | 53.165 |
| | | (46.923) | (50.674) |
| | 90% | 51.297 | 58.507 |
| | | (59.453) | (70.228) |
| | $\sigma_{\theta_{AS}}$ | 7.5917 | 7.163 |
| | | (13.203) | (12.853) |

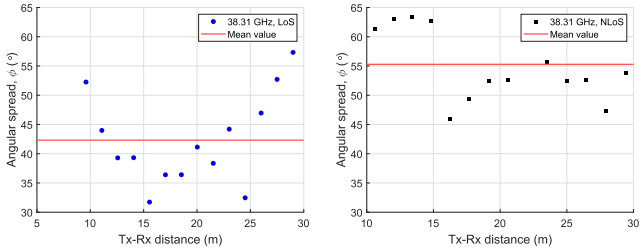


(a) 38.31 GHz.

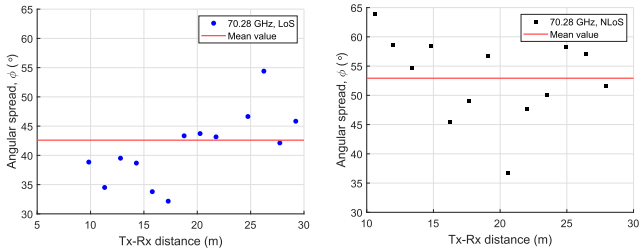


(b) 70.28 GHz.

**FIGURE 10** AS values versus Tx-Rx distance for the factory environment.

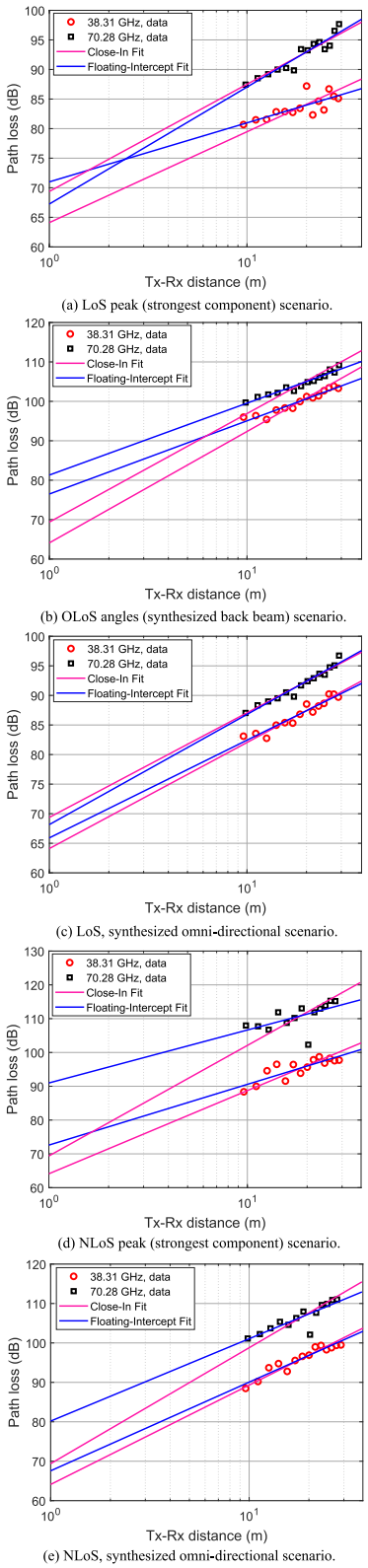


(a) LoS peak (strongest component) scenario.

(b) OLoS angles (synthesized back beam) scenario.

(c) LoS, synthesized omni-directional scenario.

(d) NLoS peak (strongest component) scenario.

(e) NLoS, synthesized omni-directional scenario.

**FIGURE 11** Path loss measurement results in LoS and NLoS scenarios for the factory environment.

### 4.1.3 | PAP and azimuth AS

Figure 8 displays the received power as a function of the azimuth rotation angles at different elevation angles across the measured bands. This figure shows an example of the calculated PAP at one of the locations in the LoS and NLoS scenarios. The azimuth AS was estimated from the PAP, where the PAP was calculated by adding the linear power for each azimuth angle over all elevation angles. The CDFs of the AS values in the industrial environment for the two measured bands at LoS and NLoS scenarios are shown in Figure 9. The

estimated AS of both bands in LoS and NLoS situations varies in a range between 30° and 65°, which is found to be similar to those obtained for indoor measurements [8, 30]. The obtained results of the AS are also larger than those reported in the outdoor environments [11, 31], as a result of the large number of reflectors and scatterers within the indoor environments. Due to the metallic surfaces on both sides of the factory scenario, it acted as a wave guide in these measurements, focusing the signals in one direction and resulting in a lower AS value. The 10%, 50%, and 90% CDF values of the angular spread and the corresponding standard deviation $\left(\sigma_{(\theta_{AS})}\right)$ are summarised in Table 4. From this table, it can be seen a maximum difference of 11°–13° between the LoS and NLoS scenarios across the measured bands for 50% of the CDF values in the industrial environment. Furthermore, a maximum difference was found less than 3° between the two measured bands for 50% of the CDF values. The table also shows that the maximum difference varied in the range of 3°–18° between the two measured bands for 50% of the CDF values in the LoS and NLoS scenarios in the office environment.

Figure 10 displays the azimuth AS values as a function of the Tx-Rx separation distance for both LoS and NLoS scenarios across the two measured bands. It can be observed that the AS values are randomly distributed around the mean value. In the NLoS case, the mean angular spread values are higher across all the distances than in the LoS case, which are 55.28° and 52.93° for 38 and 70 GHz, respectively. Additionally, the results indicate that the highest and lowest AS values occurred based on the Rx location within the environment.

### 4.1.4 | PL

Both on-the-air and back-to-back calibrations were employed to calibrate the measured data to account for the overall system gain and the antenna gains. Following calibration, single-frequency PL models were used to estimate the PL coefficients using the least square fit. In the present work, the PL was estimated for different possible antenna alignments: strongest component (the maximum received power from the main beam), synthesised back beam (the summation of the received power from the back beam), and synthesised omni-directional (the summation of the received power from all azimuth and elevation angles). The directional and omni-directional PL data were then used to estimate the PL coefficients using the CI and FI models. The omni-directional PL values were estimated from the synthesised omni-directional received power at each position, which was obtained by summing the directional received power from all rotation angles [32]. Since the angle of rotation in these measurements was less

**TABLE 5** Path loss model parameters of the CI and FI models for the factory (office) environments.

| Freq. GHz | Scenarion | PL estimation method | CI model ($\alpha$, $\sigma$) | FI model ($\alpha$, $\beta$, $\sigma$) |
|---|---|---|---|---|
| 38.31 | LoS | Strongest beam | 1.54, 1.45 | 0.99, 70.99, 1.21 |
| | | | (1.64, 2.64) | (1.16, 69.77, 2.50) |
| | | Synthesised back Beam | 2.83, 1.58 | 1.86, 76.49, 0.71 |
| | | | (2.17, 2.72) | (0.99, 78.02, 1.81) |
| | | Synthesised Omni-directional | 1.79, 0.73 | 1.65, 65.91, 0.70 |
| | | | (1.57, 2.13) | (1.03, 70.47, 1.91) |
| | NLoS | Strongest beam | 2.46, 1.94 | 1.79, 72.59, 1.68 |
| | | | (3.42, 3.28) | (2.33, 77.07, 2.68) |
| | | Synthesised Omni-directional | 2.52, 1.08 | 2.25, 67.56, 1.01 |
| | | | (3.19, 2.13) | (2.32, 74.32, 1.51) |
| 70.28 | LoS | Strongest beam | 1.81, 0.96 | 1.98, 67.25, 0.93 |
| | | | (1.83, 2.45) | (1.67, 71.27, 2.44) |
| | | Synthesised back Beam | 2.75, 1.47 | 1.82, 81.31, 0.61 |
| | | | (2.35, 2.41) | (1.18, 83.49, 1.62) |
| | | Synthesised Omni-directional | 1.77, 0.59 | 1.86, 68.16, 0.57 |
| | | | (1.71, 1.86) | (1.33, 73.95, 1.77) |
| | NLoS | Strongest beam | 3.27, 3.74 | 1.57, 90.97, 2.91 |
| | | | (4.31, 3.70) | (3.98, 73.28, 3.67) |
| | | Synthesised Omni-directional | 2.94, 2.02 | 2.09, 80.18, 1.64 |
| | | | (4.27, 2.26) | (3.58, 77.72, 1.99) |

than the 3 dB beamwidth, the additional gain induced by the overlap of the antenna pattern needs to be considered for the PL calculation.

Figure 11 displays the PL modelling results of the industrial environment at 38 and 70 GHz bands for different possible antenna orientations in LoS and NLoS situations. Table 5 provides a summary of the PL modelling parameters for the directional and synthesised omni-directional PL across the measured bands. The table shows that the synthesised omni-directional beam results in terms of the intercept coefficient ($\beta$) are close to the strongest component results for both bands, since the received power was dominated by the LoS path. This table indicates that the synthesised back beam scenario exhibits a higher PL intercept ($\beta$) compared with the strongest component scenario for both measured bands in the LoS situation. The results also show that the synthesised omni-directional beam in NLoS has a 3–12 dB higher PL intercept than in the LoS case. Furthermore, the table indicates that employing the FI model results in lower standard deviation values compared with the CI model, which implies a better fit. At the 38 and 70 GHz bands, the NLoS scenario provides a greater PLE ($\alpha$) and standard deviation than the LoS case, indicating that the signal level degraded at a faster rate as it travelled farther. Moreover, due to an increase in the attenuation and the scattering at higher frequency bands, higher PLE ($\alpha$) values were estimated in the LoS and NLoS situations at 70 GHz compared with the 38 GHz. The presented PL results at both bands are very much in line with previous work reported in [4–27, 30, 33].

## 4.2 | SIMO directional channel measurements and modelling results

### 4.2.1 | Directional PDP

For the SIMO configurations, the data were analysed to obtain the PDP of each angle for the co-polar link and the cross-polar link to investigate the impacts of both co-polarised and cross-polarised antenna configurations on different relevant channel parameters. Figure 12 presents an example of the PDP at one location in the office room environment as a function of the Rx rotation angle for different polarisations (V—V and V—H). The strong component can be observed at around −40° on the co-polar link (V—V), which corresponds to the BS angle when the Tx and Rx antennas are pointing to each other. Other peaks appear at around 150° and −60°, which correspond to the NBS angles when the Rx antenna is orientated to the opposite direction. In general, the co-polarised channels have higher received signal levels than the cross-polarised channels, as shown in Figure 12, this is due to the polarisation mismatch of the Tx and Rx antennas. In comparison to co-polarised antennas, cross-polarised antennas have a greater delay spread due to the presence of more MPCs as a result of the large number of reflections within the environment.

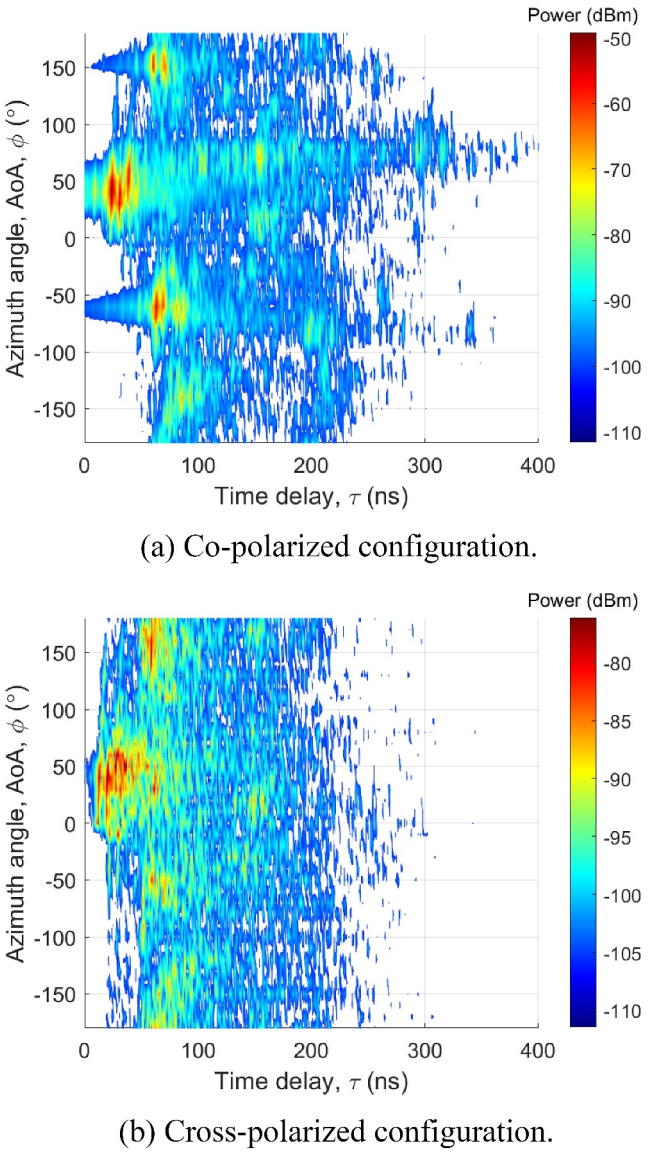


**FIGURE 12** PDP versus Rx rotation angle in conference room environment.

### 4.2.2 | RMS DS

Figure 13 displays the CDF of the RMS DS values for an office room environment. The results indicate that the OLoS case has higher RMS DS values than the LoS case. In both LoS and OLoS scenarios, the cross-polarised link has a greater delay spread value than the co-polarised link. This is due to the antenna beams being misaligned or the LoS component being obstructed, as well as the existence of several MPCs. The CDFs were fitted with a Gaussian normal distribution $N(\mu, \sigma)$ to characterise the delay spread. For each measured environment, Table 6 provides a summary of the 10%, 50%, and 90% CDF values, as well as the estimated parameter of the distribution ($\sigma$). The results also show that the standard deviation ($\sigma_{rms}$) values across all the measured scenarios for both

polarisation links are less than 13 ns. Similar results were observed for different polarisations in refs. [6–11, 30, 33].

Based on the ITU model described in Recommendation ITU-R P.1238 [29], the delay spread was modelled as a function of the surface area of the observed environment given by Equation (10). For different polarisation links, a novel model of RMS delay spread values as a function of room size ($F_s$) was generated for different possible antenna alignments. The measured RMS DS values versus different room sizes (both in $\log_{10}$-scale) are displayed in Figure 14. The solid lines in this figure indicate the linear fits of the measured RMS DS to the ITU model in different environments. The predicted model parameters based on the linear fit of the delay spread over different surface areas are shown in Table 7. The obtained results for both polarisation links at different possible antenna orientations show that the model has a positive slope ($\alpha$), indicating that RMS DS increases as the surface area increases due to an increase in scattered components. The table also shows that the root-mean-square error (RMSE) varied in a small range of 1.568 − 4.164 for both polarisation links, which indicates a better fit to the measured RMS delay spread.

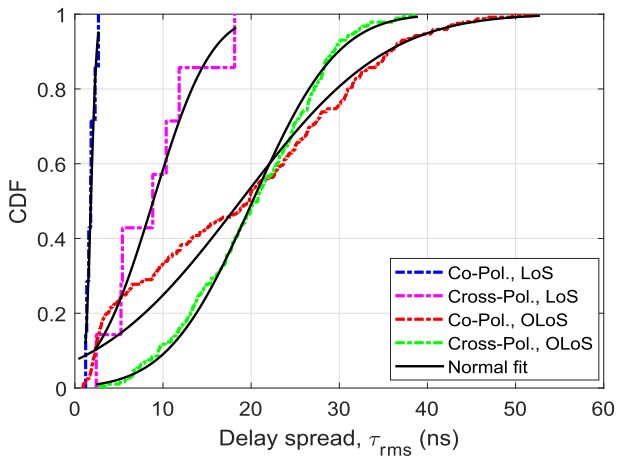


**FIGURE 13** CDF of RMS DS for conference room environment.

### 4.2.3 | PAP and azimuth AS

The azimuth angular spread was estimated from the measured PAP. Figure 15 shows an example of the computed PAP at one location for the co- and cross-polarised links in the office room environment. The CDFs of the computed AS values for the co-polarised and cross-polarised links in the office room are shown in Figure 16. This figure indicates that the

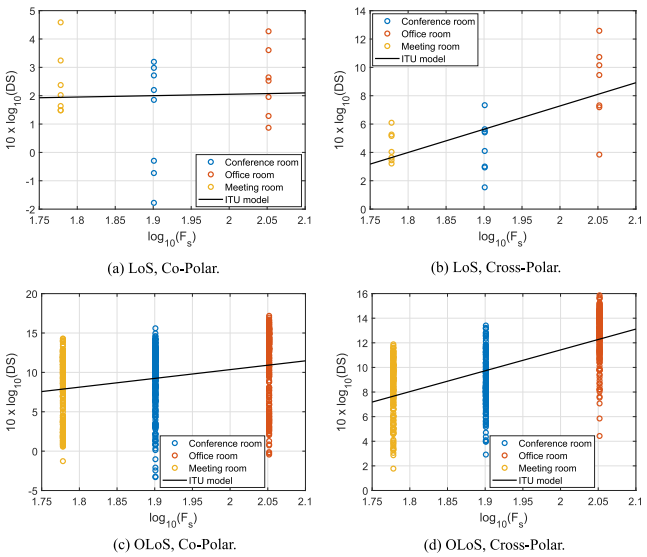


**FIGURE 14** RMS DS values versus the size of the environment (logarithmic units) based on the ITU model.

**TABLE 6** RMS DS statistics in [ns] for different measured environments.

| | | Measured scenario | | | |
|---|---|---|---|---|---|
| | | LoS | | OLoS | |
| Type of Env. | CDF of RMS DS | Co-polar | Cross-polar | Co-polar | Cross-polar |
| Conference room | 10% | 1.22 | 2.42 | 2.33 | 9.47 |
| | 50% | 1.67 | 7.11 | 19.78 | 20.52 |
| | 90% | 2.41 | 13.72 | 35.51 | 29.22 |
| | $\sigma_{rms}$ | 0.52 | 5.22 | 12.95 | 7.59 |
| Meeting room | 10% | 1.41 | 2.09 | 1.52 | 2.94 |
| | 50% | 1.53 | 2.42 | 8.14 | 7.29 |
| | 90% | 2.34 | 3.57 | 17.76 | 12.16 |
| | $\sigma_{rms}$ | 0.54 | 0.74 | 6.59 | 3.45 |
| Office room | 10% | 0.66 | 1.42 | 2.04 | 3.92 |
| | 50% | 1.53 | 2.57 | 10.07 | 6.91 |
| | 90% | 2.01 | 4.01 | 20.35 | 14.73 |
| | $\sigma_{rms}$ | 0.574 | 1.28 | 7.08 | 4.47 |

**TABLE 7** ITU model parameters for the RMS DS as a function of the room size.

| | | 59.6–56.6 GHz | | |
|---|---|---|---|---|
| **Beam direction** | **Polarisation links** | $\alpha$ | $\beta$ | **RMSE** |
| LoS | Co-polar | 0.488 | 1.074 | 1.568 |
| | Cross-polar | 16.41 | −25.55 | 2.240 |
| OLoS | Co-polar | 11.14 | −11.94 | 4.164 |
| | Cross-polar | 16.95 | −22.47 | 2.274 |

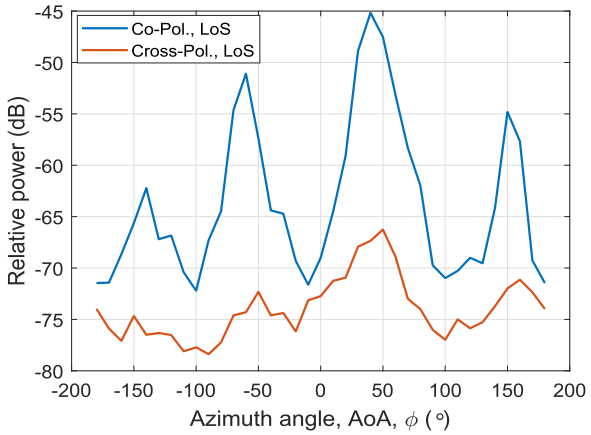


**FIGURE 15** Power angle profile in an office room environment.

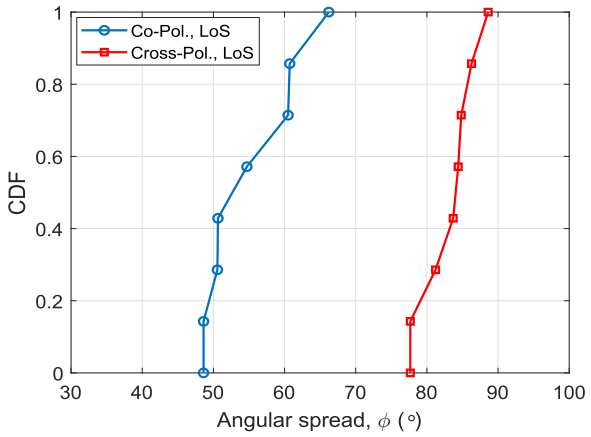


**FIGURE 16** CDF of AS for a conference room environment.

**TABLE 8** AS statistics in [degrees] for different measured environments.

| | | Measured scenario | |
|---|---|---|---|
| | | LoS | |
| **Type of Env.** | **CDF of AS** | **Co-polar** | **Cross-polar** |
| Conference room | 10% | 48.62 | 77.67 |
| | 50% | 52.67 | 84.05 |
| | 90% | 62.37 | 86.97 |
| | $\sigma_{\theta_{AS}}$ | 6.60 | 3.53 |
| Meeting room | 10% | 42.34 | 38.30 |
| | 50% | 51.81 | 54.47 |
| | 90% | 61.15 | 61.68 |
| | $\sigma_{\theta_{AS}}$ | 7.01 | 8.79 |
| Office room | 10% | 39.98 | 46.54 |
| | 50% | 45.91 | 54.33 |
| | 90% | 58.02 | 80.39 |
| | $\sigma_{\theta_{AS}}$ | 13.74 | 14.51 |

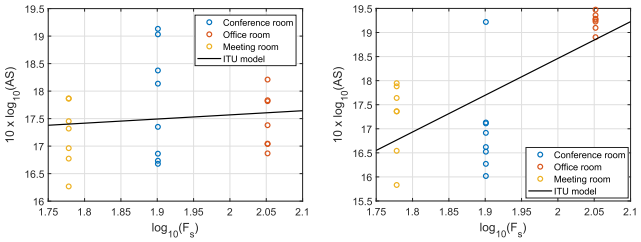


(a) LoS, Co-Polar. (b) LoS, Cross-Polar.

**FIGURE 17** AS values versus the size of the environment (logarithmic units) based on the ITU model.

**TABLE 9** The adopted model parameters for the AS as a function of the room size.

| | | 59.6–56.6 GHz | | |
|---|---|---|---|---|
| **Beam direction** | **Polarisation links** | $\alpha$ | $\beta$ | **RMSE** |
| LoS | Co-polar | 0.755 | 16.06 | 0.772 |
| | Cross-polar | 7.643 | 3.175 | 0.929 |

co-polarised link exhibits lower average AS values compared with the cross-polarised link. This might be due to the power distribution of cross-polarised links being more uniform across the angle of arrival. The 10%, 50%, and 90% CDF values of the AS and the corresponding standard deviation $(\sigma_{\theta_{AS}})$ are given in Table 8. As can be seen, the maximum difference is ~31° between the two polarised links across the measured environments for 50% of the CDF values. The results also indicate that the meeting room, which is the smallest in size, had a lower AS value, which could be due to less reflectors and scatterers. The presented AS results are very much in line with previous work reported in refs. [8, 9, 30, 33].

The angular spread was also modelled as a function of the surface area ($F_s$), according to Equation (10) where the DS is replaced by the AS, for the two polarisations and model parameters of angular spread values as a function of room size were generated. Figure 17 shows the measured AS values for the co-polarised link and the cross-polarised link at 60 GHz versus different environment sizes (both in $\log_{10}$-scale). The predicted angular spread as well as the linear fits to the ITU model are shown in this figure. Table 9 gives the estimated model parameters based on the linear fit of the angular spread values over different room sizes. The obtained results for both polarisations show that the linear fit has a positive slope ($\alpha$) or

that the AS that angular spread tends to be larger as the size of the room increases, which could be attributed to the large number of reflectors and scatterers within the room. Table 9 also shows that the RMSE is lower than 1 for both polarisation links, which indicates a good fit to the measured angular spread values.

## 5 | CONCLUSION

In this work, SISO indoor channel measurements were conducted in factory and office environments, for both LoS and NLoS scenarios at two of the frequency bands agreed in the WRC-19 for 5G wireless communication systems. The 3D data were analysed to extract different propagation channel characteristics. The presented results for all measured bands show larger RMS DS values are observed when the transmitter and the receiver antenna main beams are not aligned. Due to the large number of multipath components in an indoor environment, higher AS values were obtained in the indoor scenario for all the measured bands compared with the outdoor scenario. The PL parameters were also investigated for different possible antenna alignments using the CI and FI models, where the angular path loss coefficient was estimated from the strongest component beam, the synthesised back beam, and the synthesised omni-directional beam. Moreover, 3D SIMO dual polarised channel measurements were conducted at 60 GHz in multiple scenarios. The presented measurements aim to characterise the spatial and temporal variation of the wideband channel. It was observed that the OLoS scenario has higher RMS DS values compared with the LoS scenario when the antennas become misaligned due to the large number of obstructions and MPCs. The higher AS values emphasise the fact that indoor environments are multipath rich. The observed results also indicated that the co-polarised links exhibited lower RMS DS and AS values compared with the cross-polarised links. The relationship between the delay spread and the angular spread with the room size agrees well with the ITU model and is found to be linear with a positive slope.

## AUTHOR CONTRIBUTIONS

**Amar Al-Jzari**: Data curation; formal analysis; writing – original draft. **Sana Salous**: Conceptualisation; formal analysis; funding acquisition; methodology; project administration; resources; supervision; validation; visualisation; writing – review & editing.

## ACKNOWLEDGEMENTS

The authors would like to acknowledge the support of the WaveComBE project, under the Horizon 2020 research and innovation program with grant agreement No. 766231. The original sounder was developed under the EPSRC project PATRICIAN EP/I00923X/1, and its frequency range extended under further funding from EPSRC Impact Acceleration Account (IAA), EPSRC project mm Wave TRACCS EP/W027151/1, Ofcom, UK, and Intel, USA. The authors would also like to thank Jie Huang, Jack Tower, Mohammed Abdulali, Othman Zahid, and Saied El-Faitori at Durham University for their help in conducting the channel measurements.

## CONFLICT OF INTEREST STATEMENT

The authors declare no conflicts of interest.

## DATA AVAILABILITY STATEMENT

Measurement data for path loss are available upon request from the data bank of the ITU Study Group 3 DBSG3.

## ORCID

*Sana Salous* https://orcid.org/0000-0002-4227-9893

## REFERENCES

1. Rappaport, T.S., et al.: Millimeter wave mobile communications for 5G cellular: it will work. IEEE Access 1, 335–349 (2013). https://doi.org/10.1109/access.2013.2260813
2. Zhang, J., et al.: An experimental Study on indoor massive 3D-MIMO channel at 30-40 GHz band. In: 2018 International Symposium on Antennas and Propagation (ISAP), pp. 1–2 (2018)
3. Tercero, M., et al.: 5G systems: the mmMAGIC project perspective on use cases and challenges between 6–100 GHz. In: 2016 IEEE Wireless Communications and Networking Conference Workshops (WCNCW), pp. 200–205. Doha, Qatar (2016)
4. Haneda, K., et al.: Indoor short range radio propagation measurements at 60 and 70 GHz. In: The 8th European Conference on Antennas and Propagation (EuCAP 2014), pp. 634–638 (2014)
5. Vehmas, J., et al.: Millimeter wave channel characterization at Helsinki airport in the 15, 28, and 60 GHz bands. In: 2016 IEEE 84th Vehicular Technology Conference (VTC-Fall), pp. 1–5 (2016)
6. Maccartney, G.R., et al.: Indoor office wideband millimeter-wave propagation measurements and channel models at 28 and 73 GHz for ultra-dense 5G wireless networks. IEEE Access 3, 2388–2424 (2015). https://doi.org/10.1109/access.2015.2486778
7. Maccartney, G.R., Deng, S., Rappaport, T.S.: Indoor office plan environment and layout-based mmWave path loss models for 28 GHz and 73 GHz. In: 2016 IEEE 83rd Vehicular Technology Conference (VTC Spring), pp. 1–6 (2016)
8. Bamba, A., Mani, F., D'Errico, R.: Millimeter-wave indoor channel characteristics in V and E bands. IEEE Trans. Antennas Propagat. 66(10), 5409–5424 (2018). https://doi.org/10.1109/tap.2018.2851927
9. Bamba, A., Mani, F., D'Errico, R.: E-band millimeter wave indoor channel characterization. In: 2016 IEEE 27th Annual International Symposium on Personal, Indoor, and Mobile Radio Communications (PIMRC), pp. 1–6 (2016)
10. Raimundo, X., Salous, S., Cheema, A.: Indoor dual polarised radio channel characterisation in the 54 and 70 GHz bands. IET Microw., Antennas Propag. 12(8), 1287–1292 (2018). https://doi.org/10.1049/iet-map.2017.0711
11. Raimundo, X., et al.: Outdoor directional radio propagation measurements in the V-band. In: 2018 IEEE 29th Annual International Symposium on Personal, Indoor and Mobile Radio Communications (PIMRC), pp. 790–794 (2018)
12. Ghoraishi, M., et al.: Millimeter wave spread in delay and azimuth for small cell propagation channel at 60 GHz. In: 2017 XXXIInd General Assembly and Scientific Symposium of the International Union of Radio Science (URSI GASS), pp. 1–4 (2017)
13. Salous, S., Gao, Y.: Wideband measurements in the 60 GHz band for short range communication. In: 2016 URSI Asia Pacific Radio Science Conference (URSI AP-RASC), pp. 1–3 (2016)
14. Wu, X., et al.: 60-GHz millimeter-wave Channel Measurements and modeling for indoor office environments. IEEE Trans. Antenn. Propag. 65(4), 1912–1924 (2017). https://doi.org/10.1109/tap.2017.2669721

15. Huang, J., et al.: Multi-frequency mmWave massive MIMO Channel Measurements and characterization for 5G wireless communication systems. IEEE J. Sel. Area. Commun. 35(7), 1591–1605 (2017). https://doi.org/10.1109/jsac.2017.2699381
16. Zhu, J., Wang, H., Hong, W.: Large-scale fading characteristics of indoor channel at 45-GHz band. IEEE Antennas Wireless Propagation Lett. 14, 735–738 (2015). https://doi.org/10.1109/lawp.2014.2377952
17. Shen, Y., et al.: Millimeter-wave propagation measurement and modeling in indoor corridor and stairwell at 26 and 38 GHz. IEEE Access 9, 87792–87805 (2021). https://doi.org/10.1109/access.2021.3081822
18. Wang, Q., et al.: Wideband millimeter-wave channel characterization based on LOS measurements in an open office at 26GHz. In: 2016 IEEE 83rd Vehicular Technology Conference (VTC Spring), pp. 1–5 (2016)
19. Lei, M., et al.: 28-GHz indoor channel measurements and analysis of propagation characteristics. In: 2014 IEEE 25th Annual International Symposium on Personal, Indoor, and Mobile Radio Communications (PIMRC), pp. 208–212 (2014)
20. Zhang, L., et al.: Multifrequency wireless Channel Measurements and characterization in large indoor office environments. IEEE Trans. Antennas Propagat. 71(6), 5221–5234 (2023). https://doi.org/10.1109/tap.2023.3259736
21. Yang, W., et al.: Verification of an intelligent ray launching algorithm in indoor environments in the Ka-band. Radio Sci. 56(9), e2020RS007252 (2021). https://doi.org/10.1029/2020rs007252
22. Huang, J., et al.: Multi-frequency multi-scenario millimeter wave MIMO Channel Measurements and modeling for B5G wireless communication systems. IEEE Journals on Selected Areas 38(9), 2010–2025 (2020). https://doi.org/10.1109/jsac.2020.3000839
23. Lee, J., et al.: Measurement-based omnidirectional millimetre-wave and sub-THz propagation analysis in a large cubicle office environment. IET Microwaves Antennas and Propagations 17(6), 443–453 (2023). https://doi.org/10.1049/mia2.12363
24. Lee, J., et al.: Omnidirectional millimeter-wave propagation characteristics of corridor environments based on measurements at 28, 38, 71 and 82 GHz. In: 2022 16th European Conference on Antennas and Propagation (EuCAP), pp. 1–5 (2022)
25. Ju, S., et al.: Millimeter wave and sub-terahertz spatial statistical channel model for an indoor office building. IEEE J. Selected Areas 39(6), 1561–1575 (2021). https://doi.org/10.1109/jsac.2021.3071844
26. Xing, Y., Rappaport, T.S., Ghosh, A.: Millimeter wave and sub-THz indoor radio propagation Channel Measurements, models, and comparisons in an office environment. IEEE Commun. Lett. 25(10), 3151–3155 (2021). https://doi.org/10.1109/lcomm.2021.3088264
27. Salous, S., et al.: Wideband MIMO Channel sounder for radio measurements in the 60 GHz band. IEEE Trans. Wireless Commun. 15(4), 2825–2832 (2016). https://doi.org/10.1109/twc.2015.2511006
28. Salous, S., et al.: Radio propagation measurements and modeling for standardization of the site general path loss model in International Telecommunications Union recommendations for 5G wireless networks. Radio Sci. 55(1), e2019RS006924 (2020). https://doi.org/10.1029/2019rs006924
29. ITU-R: Recommendation ITU-R P.1238-10: Propagation Data and Prediction Methods for the Planning of Indoor Radiocommunication Systems and Radio Local Area Networks in the Frequency Range 300 MHz to 450 GHz
30. Medbo, J., Seifi, N., Asplund, H.: Frequency dependency of measured highly resolved directional propagation channel characteristics. In: 22nd European Wireless Conference, Oulu, Finland, pp. 1–6 (2016)
31. Towers, J.L., El-Faitori, S., Salous, S.: Wideband 3D performance analysis of a modular antenna array in a street canyon scenario for 5G networks. In: Antennas and Propagation Conference 2019 (APC-2019), pp. 1–6 (2019)
32. Sun, S., Maccartney, G.R., et al.: Synthesizing omnidirectional antenna patterns, received power and path loss from directional antennas for 5G millimeter-wave communications. In: 2015 IEEE Global Communications Conference (GLOBECOM), pp. 1–7 (2015)
33. Peter, M., et al.: Measurement results and final mmMAGIC channel models. Deliverable (2017)

**How to cite this article:** Al-Jzari, A., Salous, S.: Multi-band millimetre wave indoor directional channel measurements and analysis for future wireless communication systems. IET Microw. Antennas Propag. 1–14 (2024). https://doi.org/10.1049/mia2.12494